Published in final edited form as:

Radiology. 2016 December ; 281(3): 927–932. doi:10.1148/radiol.2016151447.

RF ablation, MR thermometry, and high-resolution MRI parametric mapping with a single minimally-invasive device

M. Arcan Ertürk, PhD[*,a,b], **Shashank Sathyanarayana Hegde, PhD**[*,a,c], and **Paul A. Bottomley, PhD**[a]

[a]Russell H. Morgan Dept. of Radiology, Johns Hopkins University, Baltimore, MD, USA

Abstract

Purpose—To develop and demonstrate *in vitro* and *in vivo*, a single interventional MR-active device that integrates the functions of precise identification of a tissue site with the delivery of RF energy for ablation, high-resolution thermal mapping to monitor thermal dose, and with quantitative MRI relaxometry to document ablation-induced tissue changes for characterizing ablated tissue.

Materials and Methods—All animal studies were approved by our Institutional Animal Care and Use Committee. A loopless MRI antenna comprised of a tuned micro-cable either 0.8 or 2.2mm in diameter with an extended central conductor, was switched between a 3T MRI scanner and an RF power source, to monitor and perform RF ablation in bovine muscle and human artery samples *in vitro*, and in rabbits *in vivo*. High-resolution (250–300μm) proton resonance frequency shift MR thermometry was interleaved with ablations. Quantitative spin-lattice (T_1) and spin-spin (T_2) relaxation time MRI mapping was performed pre- and post-ablation, and compared with gross tissue examination of the region of ablated tissue, post-MRI.

Results—High-resolution MRI afforded temperature mapping in under 8s for monitoring ablation temperatures exceeding 85°C delivered by the same device, producing irreversible thermal injury and necrosis. Quantitative MRI relaxation time maps revealed up to a two-fold variation in mean regional T_1 and T_2 post-vs. pre-ablation.

Conclusion—A simple, integrated, minimally-invasive interventional probe that provides image-guided therapy delivery, thermal mapping of dose and the detection of ablation-associated MRI parametric changes was developed and demonstrated. This single-device approach avoided coupling-related safety concerns associated with multiple conductor approaches.

Keywords

RF ablation; MR Thermometry; Quantitative MRI parameter mapping; Interventional MRI

[b]Currently at Center for Magnetic Resonance Research, University of Minnesota Medical School, Minneapolis, MN

[c]Currently at Philips Healthcare, Philips Innovation Campus, Bangalore, India

[*]These authors contributed equally to this work

INTRODUCTION

MRI-guided radiofrequency (RF) ablation studies have previously utilized dedicated ablation catheters for delivering RF energy, whilst monitoring treatment via relaxation-time based MRI contrast changes (1) or by MR thermometry (2–4) performed with *separate* MRI detectors. A safe ablation procedure needs to avoid hazardous coupling to the RF-applicator and/or cables while performing MRI. Furthermore, it requires fast high-resolution imaging to locate the applicator, to demarcate the target tissue and to monitor the energy delivery, as well to monitor the tissue's response at a sufficiently high spatial resolution in order to minimize potential collateral damage. The recent introduction of intravascular MRI (IVMRI) probes at magnetic field strengths of 3T and higher affords 80–300 μm transluminal resolution at speeds of up to several frames-per-second (5–8). Until now, the use of these probes was primarily limited to imaging. An earlier application to image guide and thermally-enhance gene therapy delivery at 1.5T was limited in resolution by the available signal-to-noise ratio (SNR), and did not include spin-lattice (T_1) and spin-spin (T_2) relaxation time mapping of the acute tissue response (9, 10).

Here we test whether a *single* loopless 3T MRI antenna (5, 11) can be used interchangeably to: (a) image a target site prior to RF ablation; (b) deliver RF energy for ablation; (c) monitor local temperature change using high-resolution MR thermometry; and (d) confirm tissue damage post-ablation with high-resolution relaxation-weighted and quantitative T_1 and T_2 mapping (12–14). The purpose is to develop and demonstrate *in vitro* and *in vivo*, a single interventional MR device that integrates the functions of precise identification of a tissue site with the delivery of RF energy for ablation, high-resolution thermal mapping to monitor thermal dose, and with quantitative MRI relaxometry to document ablation-induced tissue changes for characterizing ablated tissue.

METHODS

Electromagnetic and thermal simulations

The loopless antenna used in our study is an IVMRI probe designed from a miniature coaxial cable terminated with an extended inner conductor that forms a 'whip' for RF transmission/reception (9). A full-wave electromagnetic (EM) field analysis (*SEMCAD X*, Schmid & Partner Engineering AG, Zürich, Switzerland) was used by MAE (5 yrs experience with EM simulations) to compute the electric (E)-fields generated by the probe inside a homogeneous cylindrical phantom of human muscle at 128MHz (dielectric constant, 63.5; electrical conductivity, 0.72S/m). The temperature distribution induced by the E-field around the probe was calculated from the Pennes heat transfer equation (specific heat, 3421J/kg/K; thermal conductivity, 0.49W/m/K) using the SEMCAD software with a baseline temperature of 37°C, and excitations of 30, 60 and 120s at RF power levels of 10, 20, 30, and 60W during ablation. Temperature (T_e) was computed for 300s starting with each ablation. Thermal dosage was assessed from the maximum absolute temperature, and the 'cumulative equivalent minutes at 43°C' (CEM_{43}), a metric commonly used to assess thermal exposure during ablation (15). A CEM_{43} >80min can cause tissue damage in human muscle (16), while necrosis generally ensues at CEM_{43} >340min (17, 18). Tissue volumes

with $T_e \geq 42°$, 47° and 60°C, and with a CEM_{43} of 80 and 340min were used to predict ablated tissue volumes (16, 18).

Hardware and MRI acquisition

Experiments were conducted on a 3.0T whole body Philips *Achieva* MR System (Philips Medical Systems, Best, Netherlands). *In vitro* and percutaneous *in vivo* studies used a loopless antenna constructed with a 400mm-long semi-rigid copper coaxial cable (UT-85-C, Micro-coax, Inc., Pottstown, PA) with an outer diameter (OD) of 2.2mm and 39mm-long whip (SSH, 11 yrs experience with probes). *In vivo* intravascular studies employed a biocompatible loopless antenna made from 0.8mm OD nitinol hypotube with a 42mm-long whip (MAE, SSH and PAB–21 yrs experience with such probes), as pictured in Figure 1a (5). A non-magnetic RF switch connected the probe to either: (i) the MRI scanner, via a tuning-matching box, during MRI acquisition (5); or (ii) an RF power amplifier (BT00250-Gamma-CW, Tomco Technologies, Stepney, Australia (Figure 1b). The power amplifier was driven by a frequency synthesizer (PTS 160, Programmed Test Source, Littleton, MA) for performing ablations in the scanner (switching time, 3–5s), and the ablation power (128MHz, 30–60W) monitored (LB 480A, Ladybug Technologies, Santa Rosa, CA, USA) at the amplifier output.

MRI acquisitions to localize the probe relative to the ablation target, monitor probe ingress and quantitative T_1 and T_2 mapping, utilized gradient echo (GRE) turbo-spin echo (TSE) and the vendor's MIX (a combination of inversion-recovery and TSE) sequences (MAE and SSH). The vendor's analysis tools were used to compute T_1 and T_2 maps (19). MRI thermometry was performed using the proton resonance frequency (PRF)-shift method (20). A temperature coefficient of −0.01 ppm/°C was used to convert thermometric phase images acquired by the probe to temperature maps (20, 21). Large temperature changes near the probe causing 'phase-wraps' were unwrapped in the image field-of-view starting furthest (i.e., coolest) from the probe where phase-wraps were minimal, and proceeding towards it (SSH). Multiple phase-wraps at distances of < 5mm from the probe confounded the unwrapping algorithm and are color-masked in the displayed results.

MR thermometry data was compared with the numerical analysis as a function of radial distance from the probe's cable-whip junction (MAE and SSH). The pre-ablation temperature of the saline bath used for *in vitro* studies was 25°C, and a pre-ablation temperature of 35°C was assumed for the healthy rabbit *in vivo*. These base-line temperatures were added to the temperature change, ΔT_e, detected by PRF-thermometry for reporting final temperatures.

In vitro and *in vivo* experiments

In vitro experiments were performed with the semi-rigid probe inserted directly into bovine muscle specimens, and in the lumens of porcine aortas, immersed in a 3.5g/l saline bath (MAE and SSH). *In vivo* studies were approved by our Institutional Animal Care and Use Committee. Two New Zealand White rabbits were sedated with intramuscular acepromazine (1mg/kg) and ketamine (40mg/kg), induced with intravenous sodium thiopental, and intubated to maintain an open airway (SSH). In one *in vivo* protocol, the semi-rigid probe

was inserted into the thigh via percutaneous puncture. In another, the biocompatible probe was advanced into the descending aorta to the renal bifurcation (with vessel-sizes comparable to human coronary or renal arteries) via a femoral incision under contrast-enhanced X-ray computed tomography, then transferred to the MRI scanner. The scanner's 3-point-planning tool was used to prescribe a plane that contained a substantial portion of the probe. Post-mortem, the vessel-section ablated by the probe was assessed for ablation injury and discoloration by gross examination.

RESULTS

Electromagnetic and thermal-response simulations

The numerically computed temperature distribution 60s after commencing ablation at 20W power, is shown in Fig. 2(a, b). The temperature rise profiles on an axial slice centered at the probe cable-whip junction 20s post-ablation for 30, 60, and 120s-long ablations at 10, 20, and 30W of power are plotted in Fig. 2(c). The ablated area can be enlarged by increasing either the ablation-time (e.g. yellow vs. purple line, Fig. 2c) or the power level (e.g. yellow vs. brown line, Fig. 2c). Table 2 lists the volumes of tissue with temperatures of $T_e \geq 42°$, 47°, and 60°C, and with $CEM_{43} \geq 80$ and 340min. The experimentally measured temperature rise profile in bovine tissue following a 30W, 120s-long ablation (star symbols) is consistent with the computed temperature profile from the 120s-long ablation at 10W, after accounting for the cable and hardware losses (22).

In vitro and *in vivo* experiments

The pre-ablation MRI acquisitions from bovine muscle using the semi-rigid probe appear largely uniform (Fig. 3a). Ablation produced temperatures exceeding 75°C as measured by MR thermometry (Fig. 3b). The measured size of the ablated volume ($\Delta T_e > 50^{\circ}C$) was $1.5cm^3$. Post-ablation, the high-resolution MRI acquisition shows hypo-intense signal (Fig. 3c; arrow) from the ablated region, verified at gross examination post-MRI (Fig. 3d). Pre- and post-ablation T_1 maps (Fig. 3e and f, respectively) and pre- and post-ablation T_2 maps (Fig. 3g and h, respectively) show regions of heterogeneity at the ablation site (annotated ellipses), wherein T_1 is halved (320±91 vs. 182±72, Fig. 3e vs. Fig. 3f) and T_2 is doubled (96±15 vs. 197±49, Fig. 3g vs. Fig. 3h).

With the semi-rigid probe in a porcine aorta, pre-ablation MRI acquisitions at 150μm in-plane resolution depict a well-defined vessel wall (Fig. 4a). High-resolution (250μm) MR thermometry shows delivery of a 12°C thermal dose immediately above the probe (highlighted area; Fig. 4b). MRI acquisition inside a rabbit aorta *in vivo* using the biocompatible nitinol probe similarly reveals the vessel wall and surrounding tissue (Fig. 4c). High-resolution (300μm in-plane) MRI thermometry shows delivery of a ≥15°C thermal dose raising temperatures to >50°C near the probe (Fig. 4d), resulting in tissue damage confirmed by gross examination post-MRI (Fig. 4e). Some ghosting artefacts due to motion are evident in thermometry data from regions distant to the probe (Fig. 4d).

A pre-ablation MRI acquisition with the semi-rigid probe in the rabbit thigh *in vivo* is shown in Fig. 5(a). MR thermometry maps (Fig. 5b) document temperatures above 85°C near the

probe, causing an ablation confirmed at gross examination post-mortem (Fig. 5c). Pre- and post-ablation relaxometry showed T_1 increases of 18% (593±117 vs. 703 ± 193ms), while T_2 decreased by 8% (111±12 vs. 102±13ms).

DISCUSSION

In this study, we demonstrated that a single loopless antenna can be configured to acquire high-resolution MRI at 3T, locally deliver RF energy, monitor that delivery with MR-thermometry, and assess the outcome of the ablation by relaxometry. The computations show that the loopless antenna can deliver a thermal dose commensurate with the duration and RF input power level. Tissues subject to temperatures exceeding 42°C are considered thermally stressed, with temperatures above 60°C being required for tissue necrosis (18). Experimentally, we achieved temperature increases to above 85°C, resulting in irreversible tissue damage, consistent with computed thermal profiles. However, the number of studies, while demonstrating the technology, is insufficient to fully evaluate ablation efficacy. It is important to recognize that the thermal dose and the anatomical extent of the ablation will, in practice, depend on the tissue properties, including perfusion and flow. The inherent variability of this process underscores the need for a means of monitoring both the temperature rise and its ultimate effect on the surrounding tissue–in this case using the high resolution MRI thermometry and relaxometry afforded by the ablation probe itself.

Good thermal contact between the probe and the tissue is important for effective delivery of the RF energy. Temperatures >75°C produced a sizeable burn lesion in bovine muscle tissue and rabbit thigh where the probe was in direct contact with the tissue. However, temperature increases were smaller in porcine and rabbit aorta *in vitro* and *in vivo*. Here, the thermal dose and resultant injury are limited by thermal conduction in the fluid (saline or blood) within the vessel, consistent with prior observations (23). Heterogeneity in the pre-and post-ablation T_1 and T_2 maps reflect different tissue compositions (muscle, cartilage, fat etc)(24). Post-ablation, increases in T_2 *in vitro* likely reflect the response of adipose components to the heating, while the T_2 decreases seen *in-vivo* can include the effects of hemorrhage, edema, and perfusion.

In our setup, the average time to switch between RF energy delivery and MRI was 3–5s. This delay, while small compared to the total ablation periods, may cause some underestimation of the thermal dose measured by MRI thermometry. By extrapolating the PRF data, the underestimation was small (ΔT_e <3°C at a distance of 2mm from the probe). Simultaneous MRI and RF ablation at different frequencies could eliminate such underestimation with suitable RF filtering (10). Motion artefacts during parametric imaging and phase-sensitive thermal mapping sequences may be addressed using IVMRI-specific motion-correction techniques (25). The antenna design is safe for *in vivo* MRI (5), but additional anchoring in vessels may improve imaging, ablation efficiency and accuracy. The temperature changes of ΔT_e >50°C close to the probe that confounded the PRF algorithm may be solved by increasing the temporal resolution, albeit at a cost to spatial resolution.

In conclusion, we have shown that a MRI-active interventional loopless antenna at 128MHz can be configured to receive high-resolution MRI signals at 3T and locally apply RF heating

to a sample. A *single* minimally-invasive MRI probe can thus be used to perform the functions of RF ablation, high-resolution imaging and thermal monitoring of the ablation. It could thus serve as an integrated vehicle for detecting localized pathology, and the delivery and monitoring of therapy.

References

1. Lewin JS, Connell CF, Duerk JL, et al. Invited. Interactive MRI-guided radiofrequency interstitial thermal ablation of abdominal tumors: Clinical trial for evaluation of safety and feasibility. J Magn Reson Imaging. 1998; 8(1):40–47. [PubMed: 9500259]
2. Tuncali, K., Morrison, PR., Zientara, GP. MRI Monitoring and Control of Cryoablation. In: Jolesz, F., editor. Intraoperative Imaging and Image-Guided Therapy. Springer; 2014. p. 397-401.
3. Terraz, S., Salomir, R., Becker, CD. MR-Guided Radiofrequency Ablation of Liver Tumours. In: Jolesz, F., editor. Intraoperative Imaging and Image-Guided Therapy. Springer; 2014. p. 799-816.
4. Volland NA, Kholmovski EG, Parker DL, et al. Initial feasibility testing of limited field of view magnetic resonance thermometry using a local cardiac radiofrequency coil. Magn Reson Med. 2013; 70(4):994–1004. [PubMed: 23165722]
5. El-Sharkawy AM, Qian D, Bottomley PA. The performance of interventional loopless MRI antennae at higher magnetic field strengths. Med Phys. 2008; 35(5):1995–2006. [PubMed: 18561676]
6. Sathyanarayana S, Schar M, Kraitchman DL, et al. Towards real-time intravascular endoscopic magnetic resonance imaging. JACC Cardiovasc imaging. 2010; 3(11):1158–1165. [PubMed: 21071004]
7. Erturk MA, El-Sharkawy AM, Bottomley PA. Interventional loopless antenna at 7 T. Magn Reson Med. 2012; 68(3):980–988. [PubMed: 22161992]
8. Sathyanarayana S, Bottomley PA. MRI endoscopy using intrinsically localized probes. Med Phys. 2009; 36(3):908–919. [PubMed: 19378751]
9. Qiu B, Yeung CJ, Du X, et al. Development of an intravascular heating source using an MR imaging guidewire. J Magn Reson Imaging. 2002; 16(6):716–720. [PubMed: 12451585]
10. Qiu B, El-Sharkawy AM, Paliwal V, et al. Simultaneous radiofrequency (RF) heating and magnetic resonance (MR) thermal mapping using an intravascular MR imaging/RF heating system. Magn Reson Med. 2005; 54(1):226–230. [PubMed: 15968681]
11. Ocali O, Atalar E. Intravascular magnetic resonance imaging using a loopless catheter antenna. Magn Reson Med. 1997; 37(1):112–118. [PubMed: 8978639]
12. Ghugre NR, Ramanan V, Pop M, et al. Quantitative tracking of edema, hemorrhage, and microvascular obstruction in subacute myocardial infarction in a porcine model by MRI. Magn Reson Med. 2011; 66(4):1129–1141. [PubMed: 21337425]
13. Verhaert D, Thavendiranathan P, Giri S, et al. Direct T2 quantification of myocardial edema in acute ischemic injury. JACC Cardiovasc Imaging. 2011; 4(3):269–278. [PubMed: 21414575]
14. Ding H, Fernandez-de-Manuel L, Schar M, et al. Three-dimensional whole-heart T2 mapping at 3T. Magn Reson Med. 2015; 74(3):803–816. [PubMed: 25242141]
15. Moros, E. Physics of thermal therapy: fundamentals and clinical applications. Taylor & Francis; 2012.
16. Yarmolenko PS, Moon EJ, Landon C, et al. Thresholds for thermal damage to normal tissues: an update. Int J Hyperther. 2011; 27(4):320–343.
17. Graham SJ, Chen L, Leitch M, et al. Quantifying tissue damage due to focused ultrasound heating observed by MRI. Magn Reson Med. 1999; 41(2):321–328. [PubMed: 10080280]
18. Chang IA. Considerations for thermal injury analysis for RF ablation devices. Open Biomed Eng J. 2010; 4:3–12. [PubMed: 20300227]
19. den Kleef JJE, Cuppen JJM. RLSQ: T1, T2, and ρ calculations, combining ratios and least squares. Magn Reson Med. 1987; 5(6):513–524. [PubMed: 3437812]
20. Ishihara Y, Calderon A, Watanabe H, et al. A precise and fast temperature mapping using water proton chemical shift. Magn Reson Med. 1995; 34(6):814–823. [PubMed: 8598808]

21. Erturk MA, El-Sharkawy A-M, Bottomley PA. Monitoring local heating around an interventional MRI probe with RF radiometry. Med Phys. 2015; 42(3):1411–1423. [PubMed: 25735295]

22. El-Sharkawy AM, Qian D, Bottomley PA, Edelstein WA. A multichannel, real-time MRI RF power monitor for independent SAR determination. Medical Phys. 2012; 39(5):2334–2341.

23. Goldberg SN, Gazelle GS, Halpern EF, Rittman WJ, Mueller PR, Rosenthal DI. Radiofrequency tissue ablation: importance of local temperature along the electrode tip exposure in determining lesion shape and size. Academic Radiol. 1996; 3(3):212–218.

24. Gold GE, Han E, Stainsby J, Wright G, Brittain J, Beaulieu C. Musculoskeletal MRI at 3.0 T: relaxation times and image contrast. AJR Am J Roentgenol. 2004; 183(2):343–351. [PubMed: 15269023]

25. Hegde SS, Zhang Y, Bottomley PA. Acceleration and motion-correction techniques for high-resolution intravascular MRI. Magn Reson Med. 2015; 74:452–461. [PubMed: 25163750]

Advances in Knowledge

- A single multi-functional interventional MRI (IVMRI) device is developed for: image-guided localized RF ablations; monitoring thermal dose using high-resolution ($0.3\times0.3mm^2$, in plane) thermal mapping; and documenting ablation-induced parametric tissue changes on quantitative MRI.
- High-resolution (~300 μm) 3T MRI afforded temperature mapping in under 8 seconds and monitored ablation temperatures exceeding 85°C delivered by the same IVMRI device, in tissue specimens *in vitro* and *in vivo* in a rabbit model.
- Quantitative parametric maps revealed up to a *two-fold* variation in mean MRI relaxation times post- vs. pre-ablation.

Implications for Patient Care

- A single 3T MRI antenna can be used for high-resolution image-guided RF ablation and MRI thermometry and characterizing tissue response.

Summary statement

A *single* minimally-invasive MRI probe can be used to perform the functions of RF ablation, high-resolution imaging, thermal monitoring and detection of the ablation.

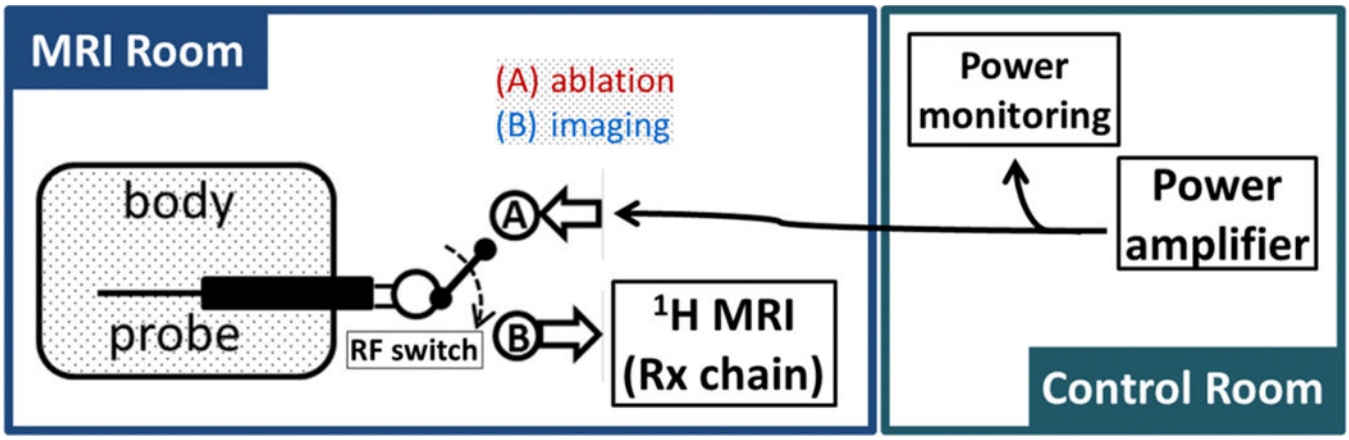

Figure 1.

(a) Photograph of the distal end of the loopless antenna used for *in vivo* studies, formed from 0.8mm OD nitinol hypotube (left) with a 42mm-long whip whip (right). (b) Schematic of a loopless antenna switchable between (A) RF ablation and (B) MRI.

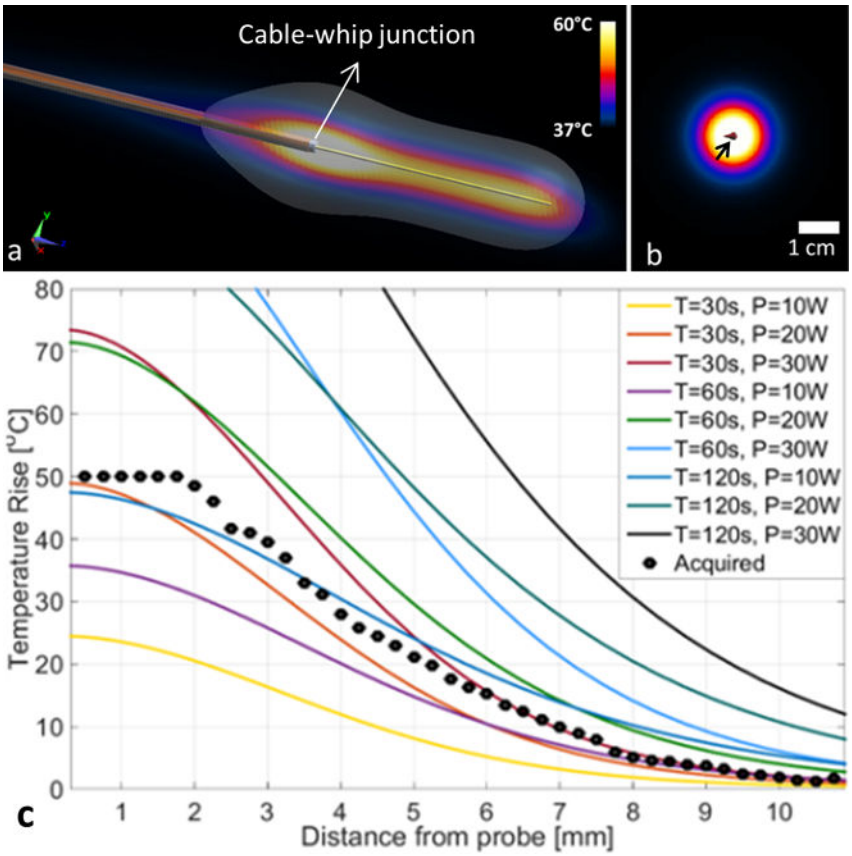

Figure 2.

(a) Computed temperature distribution 60s after termination of a T=60s-long ablation session with a power, P=20W. The cable-whip junction is annotated. Part (b) shows the temperature increase, T_e, in a axial plane perpendicular to the probe's long axis. The distribution is circularly symmetric about the probe (arrow). Part (c) shows computed temperature rise profiles 20s after termination of ablation at various power levels, P, in Watts, vs. radial distance from the probe r (solid lines). Experimental MRI thermometry data acquired from bovine muscle tissue with P=30W, and T=120s, are plotted as points (see also Fig. 3).

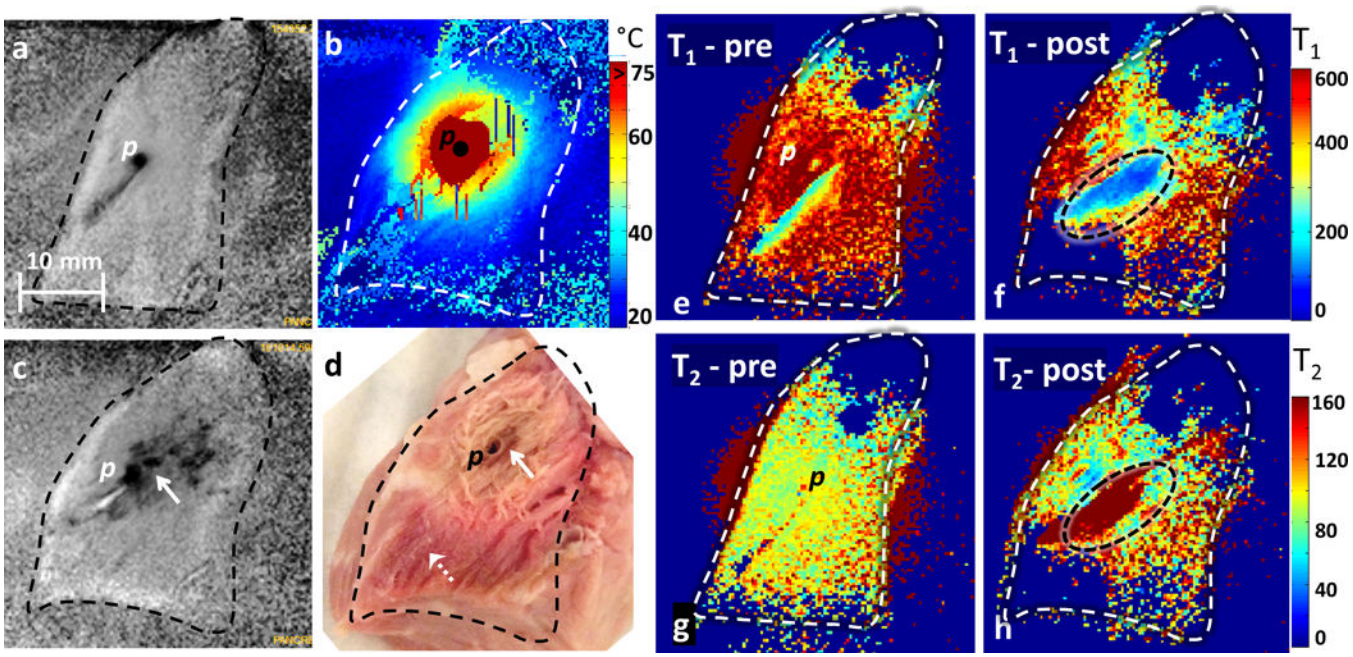

Figure 3.

(a) Pre-ablation MRI of a bovine muscle tissue (outlined with dashed line) acquired *in vitro* (*p* denotes probe location). The tissue appears homogeneous except for a hypo-intense streak near the probe. (b) Temperature distribution during ablation (P=30W, T=120s). The dark red mask around the probe corresponds to areas with temperatures T_e >75°C. (c) Post-ablation MRI from the same specimen showing a hypointense ablation lesion. (d) Brown discoloration of the lesion is evident in the gross photograph taken post-ablation (solid arrow), while unaffected tissue remains pinkish (dashed arrow). Slight changes in the shape of the tissue pre- and post-ablation are due to the effects of ablation and saline immersion. Parts (e) and (f) are corresponding transaxial T_1 images of the sample pre- and post-ablation, respectively. Parts (g) and (h) are the T_2 maps. Images (e–h) were acquired with the MIX sequence. In the elliptical annotated regions post-ablation, mean T_1 is halved (Fig. 3f) and T_2 doubled (Fig. 3h) as compared to pre-ablation. The 10mm scale bar in (a) applies to all images. Sequence parameters: (a–c) 3D gradient echo (GRE) with repetition time TR=150ms, echo time TE=5 ms, flip angle FA=40°, voxel-size =0.3×0.3×2 mm^3 and duration =69s; (b) 2D GRE with TR=50ms, TE=25 ms, FA=24°, voxel-size =0.25×0.25×6mm^3, and duration=8s; and (e-h) MIX sequence with TR=948ms, TE=22ms, inversion time TI =300 ms, FA=90°, voxel-size =0.3×0.3×2mm^3, and duration =212 s.

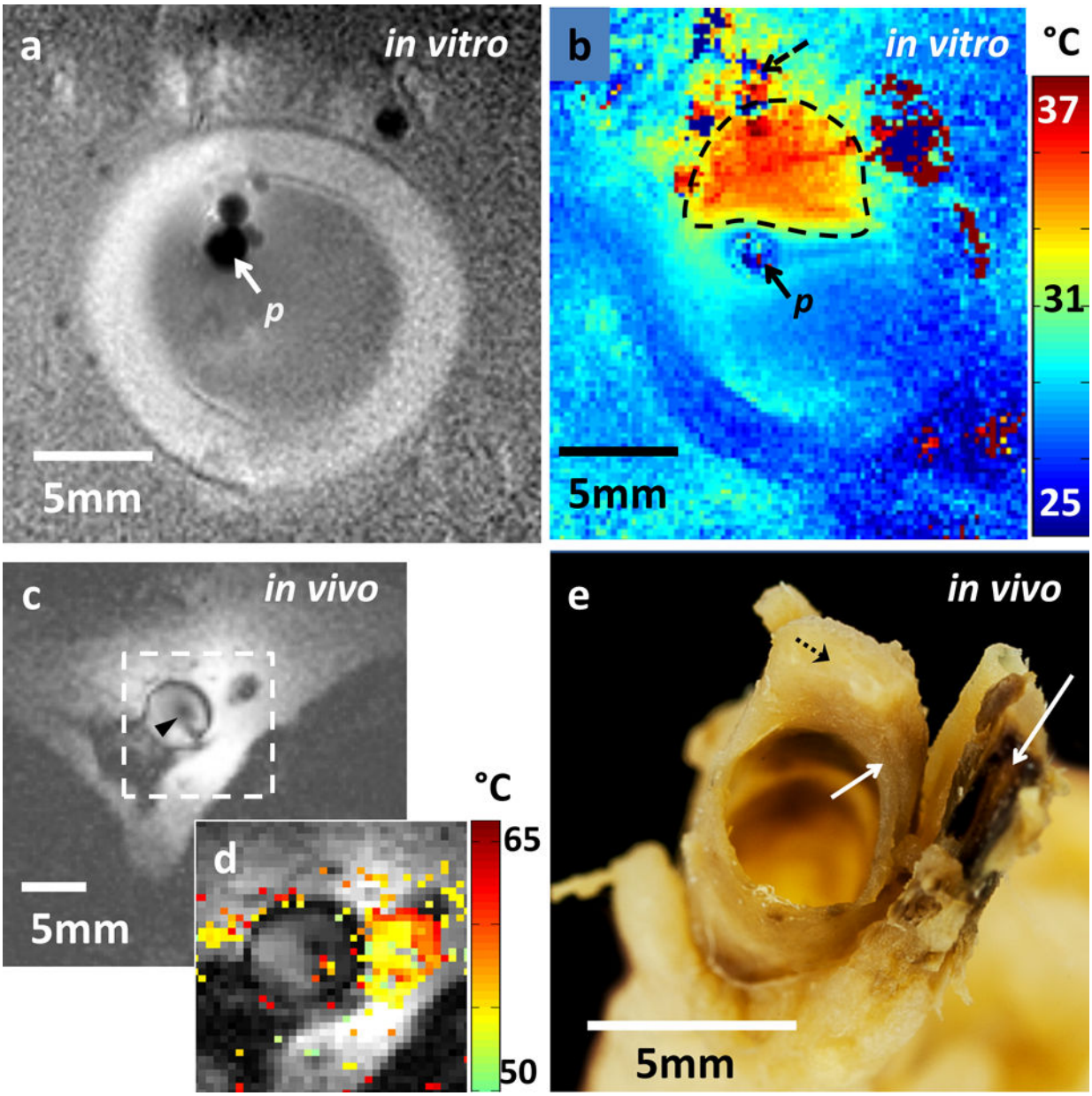

Figure 4.

(a) MRI of a porcine aorta acquired *in vitro* from probe *p* (3D turbo spin-echo, TSE; TR/TE: 1500/16 ms; voxel-size =0.15×0.15×2 mm^3; duration =170 s). **(b)** Temperature difference image (ΔT_e; °C) produced by MRI thermometry (2D GRE; TR/TE =50/25 ms; FA=25°; voxel-size =0.25×0.25×6mm^3; duration =8s) relative to a 25°C base-line temperature. The thermally affected region is annotated (dashed area). The artefact in top left (dashed arrow) above the heated area is attributed to rising thermal convection away from the ablation site, causing signal dephasing over the 8s time frame of this scan. **(c)** MRI acquired with the nitinol-probe (arrowhead) in a rabbit aorta *in vivo* annotated with a target area (dashed box; MIX sequence, TR/TE =948/22 ms; TI: 300 ms; FA =90°; voxel-size =0.3×0.3×5mm^3; duration =240 s). **(d)** ΔT_e map (°C) acquired by MRI thermometry (2D GRE, TR/TE =41/25

ms; FA =24°; voxel-size =0.3×0.3×8mm^3; duration =6s) in the target area from (c), overlaid on the MRI. **(e)** Tissue damage in vessel wall and surroundings evidenced by dark discoloration (arrows) compared to the yellow viable tissue (dashed arrow) in post-mortem photograph of the sectioned vessel.

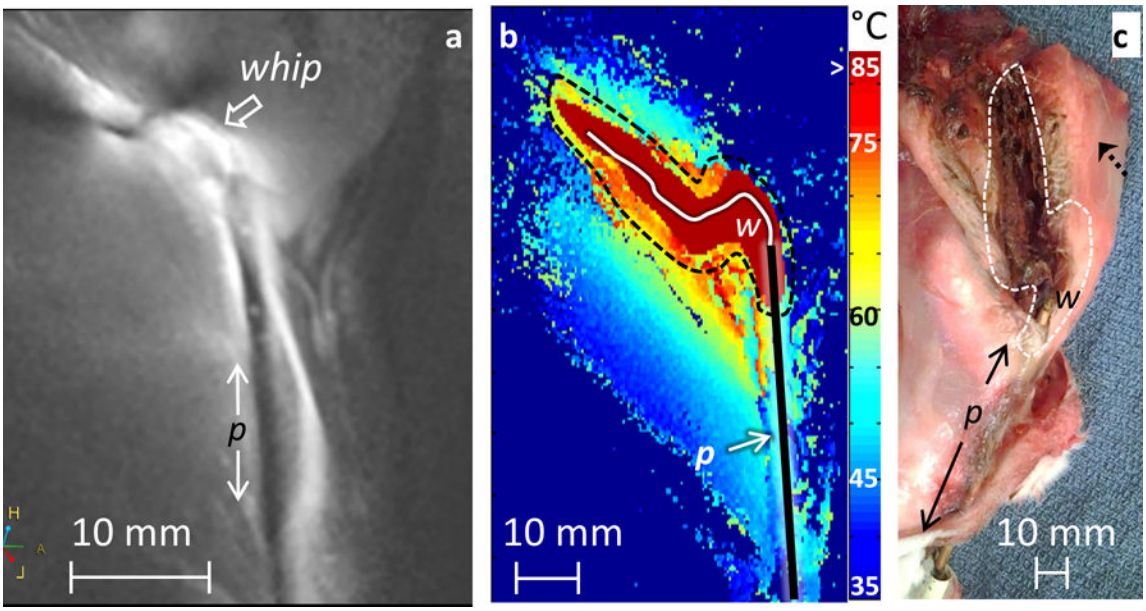

Figure 5.

In vivo percutaneous probe placement into a rabbit thigh. (a) MRI of probe location (MIX sequence, TR/TE =649/21 ms, FA =90°; voxel-size =0.3×0.3×4 mm^3; duration=160 s). The antenna *p* and whip junction locations are annotated. **(b)** MRI thermometry (2D GRE, TR/TE =42/25 ms, FA =25°; voxel-size= 0.3×0.3×8mm^3; duration =6s) during RF ablation (P=30W, T=240s) with temperatures >85°C masked (dark red) and the probe location, *p*, whip junction, *w*, and region of necrosis (dashed line) annotated. **(c)** Post-mortem photograph showing a cut through the ablated area beginning at whip junction *w* shows corresponding necrosis as brown discoloration (dashed line vs. b) compared to viable pinkish tissue (dashed arrow).

TABLE 1

Calculated tissue volumes (in cm^3) with maximum temperature greater than 42°, 47°, and 60°C; and with CEM_{43} values greater than 80 and 340 min. used to predict ablated tissue volumes (16, 18).

Ablation Duration (s)	Ablation Power (W)	Tissue volume (cm^3)				
		maximum temperature greater than:			CEM_{43} duration greater than:	
		42 °C	47°C	60°C	80 min	340 min
30	10	3.5	1.4	0.4	0.8	0.7
	20	8.0	3.5	1.2	2.5	2.0
	30	12.5	5.8	2.0	4.3	3.5
	60	26.1	12.5	4.9	10.7	8.6
60	10	7.7	3.2	0.8	2.2	1.7
	20	16.9	7.7	2.6	6.1	4.8
	30	26.0	12.3	4.6	10.5	8.4
	60	49.0	26.0	10.5	23.0	19.1
120	10	16.5	7.1	1.9	5.5	4.2
	20	33.8	16.5	5.8	14.2	11.4
	30	47.0	25.7	10.0	22.0	18.4
	60	73.0	47.0	22.1	39.8	35.0